

# The Effects of Reaction-Product Formation on the Reductive Dissolution of MnO<sub>2</sub> by Fe(II)

JOHN E. VILLINSKI,<sup>\*,†</sup>  
JAMES E. SAIERS,<sup>‡</sup> AND  
MARTHA H. CONKLIN<sup>†</sup>

Department of Hydrology and Water Resources,  
The University of Arizona, P.O. Box 210011, Tucson,  
Arizona, 85721-0011, and School of Environmental Studies,  
Yale University, New Haven, Connecticut, 06511

We conducted batch-reactor experiments to measure the reductive dissolution of pyrolusite-coated ( $\beta$ -MnO<sub>2</sub>) quartz by Fe(II) under conditions representative of an acid mine-drainage subsurface plume. The results reveal that reductive dissolution rates were initially rapid but declined considerably as Fe(III)(aq), a product of the reductive-dissolution reaction, was removed from solution by heterogeneous precipitation. The inhibition of reductive-dissolution was attributed to blocking of the  $\beta$ -MnO<sub>2</sub> surface sites by the Fe(III)(s) precipitate. Calculations of a simple model that accounts for the effects of Fe(III)(s) precipitate formation on reductive dissolution rates closely match temporal changes in Mn(II), Fe(II), and Fe(III) concentrations measured in 10 experiments, distinguished on the basis of the initial Fe(II)-to-Mn(IV) mole ratio and the initial Fe(III)(aq) concentration. The model-data comparisons reveal that the initial reaction rate on a clean  $\beta$ -MnO<sub>2</sub> surface exceeds the long-term reaction rate by 3 orders of magnitude, highlighting the importance of linking Fe(III) precipitation with the reductive dissolution of  $\beta$ -MnO<sub>2</sub> by Fe(II).

## Introduction

Manganese oxides occur ubiquitously in geologic environments as coatings on rocks, soils, and sediments. Oxidation–reduction reactions that involve these Mn oxides influence the speciation of waterborne constituents and thus play an important role in issues related to contaminant mobility and water quality. Consider, for example, oxidation–reduction reactions between pyrolusite ( $\beta$ -MnO<sub>2</sub>) and chromium. The presence  $\beta$ -MnO<sub>2</sub> increases the mobility of chromium in subsurface environments by oxidizing Cr(III), which has low solubility in natural waters (1), to Cr(VI), which has high aqueous solubility and adsorbs weakly to most geologic solids (2, 3). Manganese minerals also oxidize arsenic, transforming highly toxic As(III) to less toxic As(V) (4–6). The reductive dissolution of Mn oxides by Fe(II) has similarly significant water-quality consequences, leading to the contamination of streams and drinking water wells with Mn(II) and acidity (7).

Reactions governing the reductive dissolution of Mn oxides are made particularly complex by the formation of

reaction products that affect the extent and rate of oxidation–reduction. These rate-controlling reaction products may, under some conditions, consist of adsorbed ionic species (e.g., ref 2); however, precipitates that form over the redox-sensitive surface have been more commonly implicated as agents of oxidation–reduction inhibition (8–10). For instance, Postma (11) suggested that precipitation of an Fe(III) reaction product inhibits the reduction of birnessite ( $\delta$ -MnO<sub>2</sub>) by Fe(II), and, in a more recent study, Fendorf et al. (12) demonstrated that accumulation of an  $\alpha$ -Mn<sub>2</sub>O<sub>3</sub> surface precipitate impedes the reductive dissolution of  $\beta$ -MnO<sub>2</sub> by Co(II)-EDTA.

Although the notion that solid-phase reaction products affect the electrochemical reduction of Mn(IV) minerals is well accepted, relatively few studies have systematically examined the interactions between reaction-product formation and the kinetics of Mn(IV) reductive dissolution. In this work, we present data from batch-reactor experiments that illuminate the effects of ferric precipitate formation on the kinetics of  $\beta$ -MnO<sub>2</sub> reductive dissolution by Fe(II). These experiments were conducted under chemical conditions similar to those found in the aquifer of the Pinal Creek Basin (near Globe, Arizona), a system impacted by acid mine drainage (AMD), where oxidation–reduction reactions between  $\beta$ -MnO<sub>2</sub> and Fe(II) are known to influence groundwater and surface-water chemistry (see ref 7 and references therein). By comparing the measurements from the batch experiments with calculations of a new mathematical model, we quantify (i) the initial rates of  $\beta$ -MnO<sub>2</sub> reductive dissolution, (ii) the kinetics of Fe(III) precipitation onto the  $\beta$ -MnO<sub>2</sub> surface, and (iii) the relationship between the Fe(III)-precipitate levels and the long-term rates of  $\beta$ -MnO<sub>2</sub> reductive dissolution. These results—in particular the evaluations of the kinetics model against the experimental data—advance current understanding of how the feedbacks between reaction-product formation and reductive-dissolution govern the fate of redox-sensitive constituents in hydrogeologic environments.

## Experimental Methods

**Synthesis of  $\beta$ -MnO<sub>2</sub>-Coated Quartz.** We coated quartz sand (50–60  $\mu$ m, Iota Standard, Unimin Corp.) with  $\beta$ -MnO<sub>2</sub> (13). The presence of  $\beta$ -MnO<sub>2</sub> was confirmed by powder X-ray diffraction (XRD) and by X-ray absorbance near-edge structure spectroscopy (XANES) (Table SI-1 and Figure SI-1, respectively) (14). The average valence of the Mn on the quartz sand (herein referred to as  $\beta$ -MnO<sub>2,q</sub>, where the q indicates the presence of the quartz substrate) was determined to be  $4.01 \pm 0.02$  by the oxalate method (15). Based on multipoint N<sub>2</sub>–BET measurements before and after coating, the specific surface area of the  $\beta$ -MnO<sub>2</sub> particles equaled 19 m<sup>2</sup> g<sup>−1</sup>. The  $\beta$ -MnO<sub>2</sub> occurred as 1–2  $\mu$ m hemispherically shaped crystals on the surface of the quartz (Figure SI-2) (14). The average solid-phase concentrations of  $\beta$ -MnO<sub>2,q</sub> in two batches of sand prepared for this study, were  $7.18 \pm 0.09$  (B1) and  $6.24 \pm 0.12$  (B2) mg Mn(IV) g<sup>−1</sup> total.

**Batch Experiments with Zero-Initial Fe(III) Concentrations.** All batch experiments were performed at  $25 \pm 1$  °C in a polypropylene reactor vessel, which, in turn, was contained inside a glovebox with a 97% N<sub>2</sub>–3% H<sub>2</sub> atmosphere. The reactor vessel was fitted with a series of baffles to help suspend the Mn(IV)-coated sand and ensure even mixing (16). Batch-solution compositions (including the composition of contaminated Pinal Creek groundwater for comparison) and initial conditions are listed in Tables 1 and 2, respectively. Cation concentrations in the batch experiments were ad-

\* Corresponding author phone: (520)626-1566; fax: (520)621-1647; e-mail: john@hwr.arizona.edu. Present address: Soil, Water, and Environmental Sciences, Shantz Bldg 38, Room 429, P. O. Box 210038, The University of Arizona, Tucson, Arizona, 85721-0038.

<sup>†</sup> The University of Arizona.

<sup>‡</sup> Yale University.

**TABLE 1. Chemical Compositions of Contaminated Pinal Creek Basin Groundwater and Solutions Employed in Batch Experiments<sup>a</sup>**

constituent	contaminated groundwater <sup>b</sup>	inert electrolyte	reactive electrolyte
pH	3.30	3.00	3.00
temperature	17	25	25
dissolved O <sub>2</sub>	<0.006	<0.0004	<0.0004
Ca	11.6	6.3	6.3
Mg	15.8	93.7	85.3–89.5
Na	9.4	9.5	9.5
Fe(II)	52.4	0	4.2–8.4
Fe(III)	<2	0	0.0–3.6
SO <sub>4</sub> <sup>2-</sup>	100	102	102
Cl <sup>-</sup>	9.5	9.5	9.5
ionic strength	232	210	220

<sup>a</sup> All values in mM except for pH (standard units) and temperature (°C). <sup>b</sup> Contaminated Pinal Creek Basin groundwater composition from ref 7. Other constituents in the contaminated groundwater include (mM) the following: K = 0.2, Mn = 1.34, Al = 10.5, Cu = 2.4, Co = 0.20, Ni = 0.06, and Zn = 0.33.

**TABLE 2. Initial Conditions of the Batch-Reactor Experiments**

expt no. (batch)	Mn(IV)(s) <sup>a</sup> (mM)	Fe(II)(aq) (mM)	Fe(III)(aq) (mM)	Fe(II): Mn(IV) <sub>init</sub> <sup>b</sup>	duration (h)
1 (B1)	3.66	7.65	0	2.09 ± 0.11	71.6
2 (B1)	3.75	8.38	0	2.23 ± 0.12	6.0
3 (B1)	3.19	7.31	0	2.29 ± 0.12	2.0
4 (B2)	3.16	8.38	0	2.66 ± 0.14	5.4
5 (B2)	5.94	8.38	0	1.41 ± 0.08	6.0
6 (B1)	5.97	8.38	0	1.40 ± 0.08	6.0
7 (B1)	3.66	4.19	0	1.14 ± 0.06	5.5
8 (B1)	3.66	7.25	1.66	1.98 ± 0.10	75.0
9 (B1)	3.66	7.60	3.58	2.07 ± 0.11	21.5
10 (B1)	3.39	7.30	3.63	2.15 ± 0.12	4.0

<sup>a</sup> Estimated error in initial Mn(IV)(s) loading is ±2%. <sup>b</sup> Refers to the initial Fe(II)-to-Mn(IV) mole-loading ratio.

justed relative to the composition of contaminated Pinal Creek Basin groundwater: (1) no trace metals were included to focus on the Fe–Mn chemistry; (2) the Fe(II) concentration was reduced from 52.4 mM to 4.2–8.4 mM in order to maintain nearly stoichiometric proportions (1.14–2.66) with Mn(IV)(s) (Mn(IV)(s) concentrations were limited by the ability to suspend the sand particles); (3) the Ca concentration was reduced for solubility considerations; and (4) the Mg concentration was increased such that the ionic strength of the batch solutions approximated that of contaminated Pinal Creek Basin groundwater.

The first step of the batch experiments involved suspending 4.9–10.6 g of  $\beta$ -MnO<sub>2,q</sub> in 190–200 mL of inert electrolyte at pH 3.00 (see Table 1). After the suspension had equilibrated for 17 h, a 10 mL sample was collected to quantify the total amount of Mn released to solution. The Mn concentration in solution (prior to Fe(II) introduction) did not exceed 1 mg L<sup>-1</sup> and was identified as Mn(IV) by the oxalate method. At this low level (i.e., < 1% of the total Mn(IV)), the released, fine particulate Mn(IV) would not significantly affect reaction rates.

Following the equilibration period, Fe(II) solution was added to bring the volume to 200 mL ( $t = 0$ ), whereupon sampling was initiated within 60 s for analysis of aqueous-phase metal concentrations. (See Table 2 for initial concentrations of Fe(II).) Sampling from the well-stirred reactor removed roughly equal proportions of solution and  $\beta$ -MnO<sub>2,q</sub>. Three mL aliquots were filtered through 0.22  $\mu$ m polyacetate filters (Millipore Corp., Inc.), with the first 1.5 mL filtered to waste. This process required 10–12 s; therefore, the error in

the sampling time was  $\pm 6$  s. Iron(II) concentrations were determined from absorbance measurements made at 510 nm (Shimadzu PC2100 spectrophotometer) using the  $\alpha$ -phenanthroline method (17). Total manganese (Mn<sub>T</sub>) and total Fe (Fe<sub>T</sub>) were measured using flame atomic absorption spectrometry (Perkin-Elmer 3100). The error for both of these techniques equaled  $\pm 5\%$  or less based on calibration standards. Analysis of the batch samples by the oxalate method (15) indicated that the aqueous manganese existed entirely as Mn(II). The Fe(III)(aq) concentration was calculated as the difference between measured Fe<sub>T</sub> and Fe(II)(aq) concentrations; the error is expected to be  $\pm 7\%$  or less based on propagation of errors.

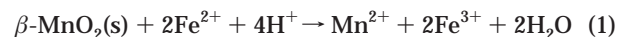
The pH of the reaction was maintained by two computer-controlled pH stats containing 0.11–0.15 M NaOH and 1.0 M H<sub>2</sub>SO<sub>4</sub>. The addition of the acid and base to the system reduced the sand-to-solution ratio. Depending on the experimental treatment, the calculated dilution ranged from 4 to 9% of the initial volume.

**Batch Experiments with Fe(III) Added Prior to Reaction Initiation.** Three experiments were conducted by adding an aliquot of an Fe(III)-SO<sub>4</sub> solution to a  $\beta$ -MnO<sub>2,q</sub>-inert electrolyte mixture prior to the addition of Fe(II). The initial Fe(III) concentrations ranged from 1.66 to 3.63 mM (Table 2). Immediately following the addition of the Fe(III), base was added to bring the solution pH to 3.00 (within one min), whereupon the pH remained stable for more than 25 min (i.e., no more base was added). The aqueous Fe(III) concentrations during this 25-minute time interval were constant within experimental error, indicating that Fe(III) adsorption and precipitation were insignificant and the solutions were supersaturated with respect to schwertmannite (i.e., the solubility-controlling Fe(III) mineral). At 30 min, Fe(II) was added (as in the Fe(II)-only experiments), and the procedures described above were employed to monitor the aqueous chemistry.

## Mathematical Model

**Overview.** We present a model appropriate for simulating the temporal variations in the concentrations of  $\beta$ -MnO<sub>2</sub>(s), Fe(II)(aq), Fe(III)(aq), Mn(II)(aq), and Fe(III)(s) under the conditions observed in our batch-reactor experiments. It is not our goal to develop a mechanistic model that incorporates the entire network of physical mass-transfer processes and elementary chemical reactions controlling oxidation–reduction. This approach would prove intractable from the standpoint of parameter estimation. Rather, our objective is to derive a parametrically simple model that can simulate the effects of reaction-product formation on the variation in the overall rates of  $\beta$ -MnO<sub>2</sub> reductive dissolution.

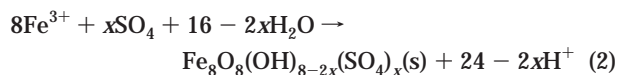
The rate laws that govern the mathematical model are based on overall (balanced) reactions for  $\beta$ -MnO<sub>2</sub> reductive dissolution and heterogeneous precipitation of Fe(III)(aq). The reductive dissolution of  $\beta$ -MnO<sub>2</sub> by Fe(II) is represented by (e.g., ref 18)



The log K for this reaction, as calculated from the thermodynamic constants in ref 19, is 15.3.

Chemical analyses of digestions of the remaining solids after dialysis with DI water indicates that the Fe(III) precipitate in our experiments had a composition similar to the mineral schwertmannite (14), and XRD analysis suggests that the precipitate was either schwertmannite or a sulfate-substituted ferrihydrite. While identification of the structure of the Fe(III) precipitate is not requisite to the model development, we assume, in accordance with published research on AMD systems (20), that schwertmannite controls Fe(III) solubility.

The stoichiometric reaction for schwertmannite precipitation is



where  $1.0 \leq x \leq 1.85$ .

Examination of SEM micrographs of the reacted  $\beta$ - $\text{MnO}_2$ -coated sand show that the Fe(III) precipitate accumulated over the  $\beta$ - $\text{MnO}_2$  crystals (Figure SI-3). We hypothesize that the Fe(III) precipitate affects the rate of reaction 1 by physically blocking access of Fe(II) to the redox-reactive sites on the  $\beta$ - $\text{MnO}_2$  surface, and we describe this inhibition with a Langmuir-type blocking function, as advanced by Sayers et al. (21) and Guha et al. (22). Our contention that ferric precipitation influences the rate of reaction 1 is supported by preliminary batch experiments in which reductive-dissolution inhibition was not observed when fluoride ( $\text{F}^-$ ) was added to the batch reactor to prevent Fe(III) precipitation. MINTEQA calculations (23) indicate that  $\text{F}^-$  formed aqueous complexes with over 98% of the Fe(III) produced during reductive dissolution, resulting in no measurable loss of Fe from solution (due to precipitation or adsorption). The data from these experiments, unlike the data from the fluoride-free experiments (where ferric precipitation did occur), could be quantified with a simple second-order rate law, without any sort of blocking function.

In formulating reactions 1 and 2, we have accounted for neither aqueous-complexation reactions with  $\text{SO}_4^{2-}$  and  $\text{Cl}^-$  nor multiple surface complexes. These simplifications are reflected in the mathematical model by lumped coefficients that effectively average between-species variability in reaction kinetics. We emphasize that this approach is consistent with the goal of the modeling component of the study, which is to use the model as a diagnostic tool to quantify the overall rates of reaction observed in the batch experiments.

**Governing Equations.** Consideration of the stoichiometry of reaction 1 leads to a rate expression for the reductive dissolution of  $\beta$ - $\text{MnO}_2$

$$-\frac{1}{V} \frac{d[\beta\text{-MnO}_2(\text{s})] V}{dt} = -\frac{1}{2V} \frac{d[\text{Fe(II)(aq)}] V}{dt} = \frac{1}{V} \frac{d[\text{Mn(II)(aq)}] V}{dt} = \frac{1}{2V} \frac{d[\text{Fe(III)(aq)}] V}{dt} = k_{r1} [\beta\text{-MnO}_2(\text{s})]^a [\text{Fe(II)(aq)}]^b \beta \quad (3)$$

where the square brackets denote constituent levels expressed in terms of aqueous concentrations (mM),  $t$  is time (h),  $k_{r1}$  is the forward reaction rate coefficient ( $\text{mM}^{1-(a+b)} \text{h}^{-1}$ ),  $\beta$  accounts for the effects of Fe(III) precipitate formation on the reaction rate, and the exponents  $a$  and  $b$  express the rate dependence on reactant concentrations. Equation 3 has been modified for dilution (due to acid and base addition) by expressing fluid volume ( $V$ ) as a function of time. The parameter  $k_{r1}$  applies to the overall reaction given by (1) and hence it measures the sum of the rates associated with the individual steps of the reductive-dissolution process. These steps include adsorption of Fe(II) to the  $\beta$ - $\text{MnO}_2$  surface, the electron-transfer reactions, and the release of reduced manganese and the oxidized iron species into solution. Both  $a$  and  $b$  are set equal to unity, thereby testing the assumption that the reductive dissolution rate is first-order with respect to both  $\beta$ - $\text{MnO}_2(\text{s})$  and  $\text{Fe(II)(aq)}$  concentrations. This assumption is reasonable in light of recent research that demonstrates a linear relationship between the kinetics of  $\beta$ - $\text{MnO}_2$  reduction by Co(II)-EDTA and the product of the  $\beta$ - $\text{MnO}_2$  and Co(II)-EDTA concentrations (21). Furthermore, the assumption of  $a = b = 1$  proved valid for simulating

reductive-dissolution kinetics in preliminary batch experiments in which  $\text{F}^-$  was added to prevent ferric-iron precipitation.

The decline of the dissolution reaction rate with the accumulation of the ferric precipitate is described in terms of a Langmuir-type blocking function

$$\beta = \max \left( 1 - \tau \frac{[\text{Fe(III)(s)}]}{[\beta\text{-MnO}_2(\text{s})]}, \beta_f \right) \quad (4)$$

where  $\tau$  is an adjustable parameter that describes the efficiency of Fe(III)(s) in occluding reactive Mn(IV) surface sites and  $\beta_f$  is an adjustable parameter with a value between zero and unity.  $\beta$  decreases from unity toward its minimum value of  $\beta_f$  as the ratio of  $[\text{Fe(III)(s)}]$  to  $[\beta\text{-MnO}_2(\text{s})]$  increases, which, according to eq 3, promotes a corresponding decrease in the rate of  $\beta$ - $\text{MnO}_2$  reductive dissolution. Once  $\beta = \beta_f$ , the kinetics of the dissolution reaction can be quantified by a second-order rate coefficient, defined as  $k_{rf} = k_{r1} \times \beta_f$ .

Given that pH is constant and sulfate is present at concentrations an order of magnitude greater than the other reactants, the temporal changes in Fe(II)(aq) and Fe(III)(s) concentrations due to ferric-iron precipitation can be expressed by

$$-\frac{1}{V} \frac{d[\text{Fe(III)(aq)}] V}{dt} = \frac{1}{V} \frac{d[\text{Fe(III)(s)}] V}{dt} = k_{r2} [\text{Fe(III)(aq)}]^n \quad (5)$$

where  $k_{r2}$  is the forward reaction rate coefficient ( $\text{mM}^{1-n} \text{h}^{-1}$ ) and  $n$  expresses the reaction rate dependence on the Fe(III)(aq) concentration. Published values of  $n$  for the heterogeneous precipitation of ferric iron are unavailable; therefore, we determine  $n$  through optimization.

The complete set of equations appropriate for quantifying the effects of ferric iron precipitation on the reductive dissolution of  $\beta$ - $\text{MnO}_2$  by Fe(II) can be obtained by combining the relationships given in eqs 3–5, such that

$$\frac{d[\beta\text{-MnO}_2(\text{s})]}{dt} = -k_{r1} [\beta\text{-MnO}_2(\text{s})] [\text{Fe(II)(aq)}] \beta - \frac{[\beta\text{-MnO}_2(\text{s})]}{V} \frac{dV}{dt} \quad (6)$$

$$\frac{d[\text{Fe(II)(aq)}]}{dt} = -2k_{r1} [\beta\text{-MnO}_2(\text{s})] [\text{Fe(II)(aq)}] \beta - \frac{[\text{Fe(II)(aq)}]}{V} \frac{dV}{dt} \quad (7)$$

$$\frac{d[\text{Mn(II)(aq)}]}{dt} = k_{r1} [\beta\text{-MnO}_2(\text{s})] [\text{Fe(II)(aq)}] \beta - \frac{[\text{Mn(II)(aq)}]}{V} \frac{dV}{dt} \quad (8)$$

$$\frac{d[\text{Fe(III)(aq)}]}{dt} = 2k_{r1} [\beta\text{-MnO}_2(\text{s})] [\text{Fe(II)(aq)}] \beta - k_{r2} [\text{Fe(III)(aq)}]^n - \frac{[\text{Fe(III)(aq)}]}{V} \frac{dV}{dt} \quad (9)$$

$$\frac{d[\text{Fe(III)(s)}]}{dt} = k_{r2} [\text{Fe(III)(aq)}]^n - \frac{[\text{Fe(III)(s)}]}{V} \frac{dV}{dt} \quad (10)$$

The derivative  $dV/dt$  was approximated by fitting a linear regression through a plot of  $t/(V - V_{\text{init}})$  versus  $t$  and differentiating the resulting expression (14). The relative error in the calculated volume was not more than  $\pm 1.5\%$ . Eqs 6–10



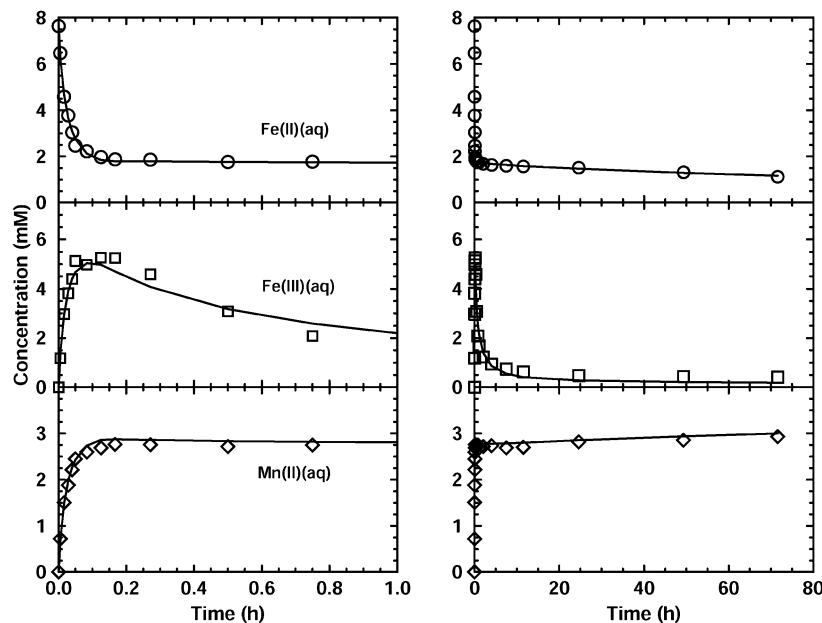


FIGURE 1. Experimental observations (open symbols) and model calculations (solid line) for experiment 1 ( $\text{Fe(II):Mn(IV)}_{\text{init}} = 2.09$ ). Experimental conditions are listed in Table 2, and the best-fit values of  $k_{r1}$ ,  $k_{r2}$ ,  $n$ ,  $\tau$ , and  $\beta_I$  are shown in Table 4.

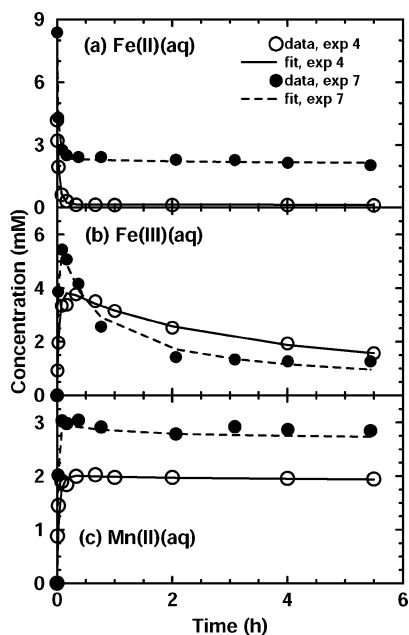


FIGURE 2. Experimental observations and model calculations for experiment 4 ( $\text{Fe(II):Mn(IV)}_{\text{init}} = 2.66$ ) and experiment 7 ( $\text{Fe(II):Mn(IV)}_{\text{init}} = 1.14$ ). Experimental conditions are listed in Table 2, and the best-fit values of  $k_{r1}$ ,  $k_{r2}$ ,  $n$ ,  $\tau$ , and  $\beta_I$  are shown in Table 4.

were solved numerically using an implicit Runge–Kutta scheme (24).

## Results and Discussion

**Experiments with Zero Initial Fe(III) Concentrations.** We observed similar trends in the temporal changes in measured reactant and product concentrations for the seven experiments with zero initial Fe(III) concentrations (i.e., experiments 1–7, Table 2). The time-series data are presented for experiment 1 (Figure 1) and experiments 4 and 7 (Figure 2), which cover the range of initial Fe(II)/Mn(IV) mole-loading ratios tested in this study (Table 3;  $\text{Fe(II):Mn(IV)}_{\text{init}}$ ). Results of the experiments demonstrate that the  $\beta\text{-MnO}_2$  reductive-dissolution rate decreased nonlinearly with time. For example, in experiment 1, where  $\text{Fe(II):Mn(IV)}_{\text{init}} = 2.09$ ,

TABLE 3. Experimental Results of the Batch Reactor Experiments

expt no.	$\text{Fe(II):Mn(IV)}_{\text{init}}$	$\text{Fe(II)}_c:\text{Mn(II)}_r^a$	$[\text{Fe(III)(aq)}]_{\text{max}}^b$ (mM)
1	$2.09 \pm 0.11$	$2.07 \pm 0.14$	4.60
2	$2.23 \pm 0.12$	$1.95 \pm 0.14$	4.12
3	$2.29 \pm 0.12$	$1.97 \pm 0.14$	4.62
4	$2.66 \pm 0.14$	$1.99 \pm 0.14$	5.44
5	$1.41 \pm 0.08$	$1.96 \pm 0.14$	5.89
6	$1.40 \pm 0.08$	$2.00 \pm 0.14$	7.14
7	$1.14 \pm 0.06$	$2.01 \pm 0.14$	3.78
8	$1.98 \pm 0.10$	$2.10 \pm 0.15$	4.92
9	$2.07 \pm 0.11$	$2.06 \pm 0.14$	6.32
10	$2.15 \pm 0.12$	$2.13 \pm 0.15$	6.86

<sup>a</sup> Molar ratio of Fe(II) consumed ( $\text{Fe(II)}_c$ ) to Mn(II) released to solution ( $\text{Mn(II)}_r$ ) at the end of the reaction. <sup>b</sup> Maximum observed Fe(III)(aq) concentration.

reductive dissolution of  $\beta\text{-MnO}_2$  released 71% of the Mn(IV) as Mn(II) during the first 0.1 h of reaction, but only 14% during the remaining 71.5 h of the experiment (Figure 1). As predicted by the stoichiometry of reaction 1, the ratio of the moles of Fe(II) consumed to the moles of Mn(II) released to solution (Table 3;  $\text{Fe(II)}_c:\text{Mn(II)}_r$ ) are statistically equal to two for experiment 1 as well as for the experiments 2–7. Aqueous Fe(III) concentrations climbed during the first 0.15 h of each experiment, peaking between 4.12 mM and 7.14 mM (Table 3;  $[\text{Fe(III)(aq)}]_{\text{max}}$ ). Concentrations remained at peak levels for only a short time before beginning a gradual decline, signaling the removal of Fe(III)(aq) from solution by precipitation and, to a much lesser extent, by adsorption (Figures 1 and 2). The onset of Fe(III) precipitation occurred as Mn(II) and Fe(II) concentrations began to stabilize, revealing a close link between ferric-precipitate formation and the decline in reductive-dissolution rates.

**Experiments with Fe(III) Added Prior to Reaction Initiation.** Except for the presence of Fe(III)(aq) at concentrations ranging from 1.66 mM to 3.63 mM, the initial conditions in experiments 8–10 resembled those in experiment 1 (Table 2). The Mn(II) and Fe(II) concentration profiles for experiments 8–10 are similar in shape to the corresponding profiles for experiment 1 but differ in magnitude (Figure 3). The percentage of Mn(II) released to solution

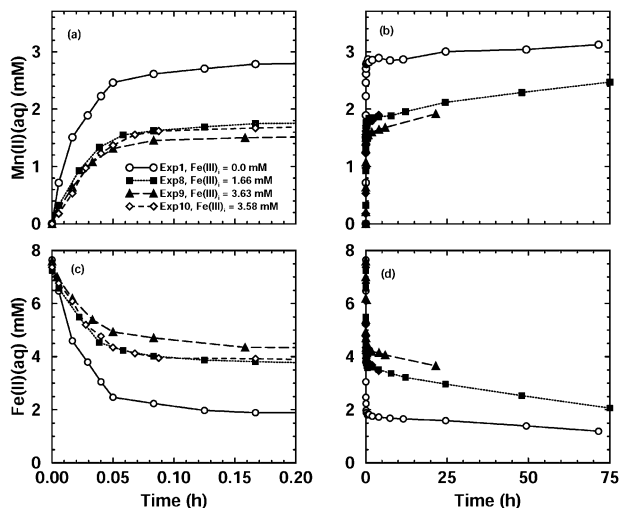


FIGURE 3. Influence of initial Fe(III) concentration on (a, b) release of Mn(II) into solution and (c, d) consumption of Fe(II)(aq).

during the first 0.15 h of reaction decreased from 76% in experiment 1, where initial Fe(III)(aq) concentrations equaled zero, to 41–47% in experiments 8–10, where Fe(III) was added to solution prior to initiation of the redox reaction (Figure 3a). After the initial 0.15 h of rapid reaction, the rates of Mn(II) release and Fe(II) consumption were similar (Figure 3 (parts b and d)), and the mass of Mn(II) released varied in stoichiometric proportions with the mass of Fe(II) consumed (Table 3;  $\text{Fe(II)}_c:\text{Mn(II)}_r$ ).

**Comparison of Experimental Results with Model Calculations.** We tested the kinetics model in inverse mode by adjusting values of  $k_{r1}$ ,  $k_{r2}$ ,  $n$ ,  $\tau$ , and  $\beta_f$  such that numerical solutions to eqs 6–10 fit the time-series data on Mn(II)(aq), Fe(II)(aq), and Fe(III)(aq) concentrations. We identified optimal parameter values by using a Levenberg–Marquardt least squares algorithm to minimize an objective function, defined as the sum-of-the-squared residuals between measured Fe(II)(aq), Mn(II)(aq), and Fe(III)(aq) concentrations and corresponding model-calculated concentrations. To simplify the parameter estimation procedure, an average  $\beta_f$  value, determined from the three long-term experiments (i.e.,

experiments 1, 8, 9), was used to simulate reaction kinetics in the seven experiments with durations less than or equal to 6 h (i.e., experiments 2–7, 10).

The model closely reproduces the temporal changes in aqueous metals concentrations, measured both in experiments with zero initial Fe(III) concentrations (Figures 1 and 2) and in experiments with Fe(III)(aq) initially present (Figure 4). Calculated model efficiencies ( $E_{\text{Mn2}}$ ,  $E_{\text{Fe2}}$ , and  $E_{\text{Fe3}}$ ), representing normalized measures of the goodness of model fit to data on Mn(II)(aq), Fe(II)(aq), and Fe(III)(aq) concentrations, exceed 0.98 for all experiments (Table 4).

The best-fit estimates of the rate coefficient for reductive dissolution ( $k_{r1}$ ) range from  $2.35 \text{ mM}^{-1} \text{ h}^{-1}$  to  $8.58 \text{ mM}^{-1} \text{ h}^{-1}$  for the seven treatments with zero initial Fe(III)(aq) concentration (Table 4). The variation in  $k_{r1}$  between the experiments does not arise from differences in the rate of electron transfer (which is an elementary-reaction step that cannot be resolved by our model) but reflects differences in the kinetics of other processes that affect the overall reaction rate, such as adsorption and desorption. These component processes of the overall reaction are sensitive to initial solution composition and solution-composition evolution, both of which vary between experiments. The average of the best-fit estimates of  $k_{r1}$  for the seven treatments with zero initial Fe(III)(aq) concentration ( $4.74 \pm 2.32 \text{ mM}^{-1} \text{ h}^{-1}$ ) is more than a factor of 2 greater than the average of  $2.05 \pm 0.15 \text{ mM}^{-1} \text{ h}^{-1}$  determined for the three experiments with nonzero initial Fe(III)(aq) concentration (Table 4). We attribute the comparatively lower (overall) rates of reductive dissolution in experiments with initial Fe(III)(aq) concentration greater than zero to enhanced competition between Fe(III)(aq) and Fe(II)(aq) for redox-reactive sites on the Mn(IV) surface. A high negative correlation between instantaneous reaction rates (estimated from second-order Lagrangian interpolation) and Fe(III)(aq) concentration supports this contention (14).

Inclusion of the blocking function (eq 4) in the model proved critical to accurate simulation of the  $\beta$ -MnO<sub>2</sub> dissolution kinetics, as model calculations made without the blocking function substantially overpredicted the mass of  $\beta$ -MnO<sub>2</sub> converted to Mn(II)(aq). Two parameters govern the blocking function:  $\tau$  and  $\beta_f$ . The parameter  $\tau$  expresses the ratio of the molar mass of  $\beta$ -MnO<sub>2</sub> blocked from reaction to the molar mass of Fe(III)(s) precipitated. The best-fit values

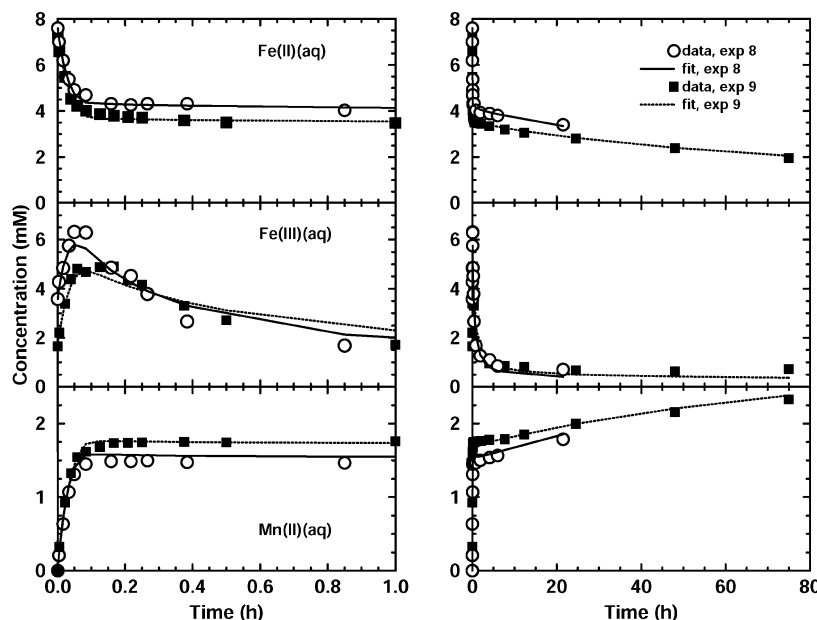


FIGURE 4. Experimental observations and model calculations for experiment 8 ( $\text{Fe(II)}:\text{Mn(IV)}_{\text{init}} = 1.98$ , initial Fe(III)(aq) concentration = 1.66 mM) and experiment 9 ( $\text{Fe(II)}:\text{Mn(IV)}_{\text{init}} = 2.07$ , initial Fe(III)(aq) concentration = 3.63 mM). Other experimental conditions are listed in Table 2, and best-fit values of  $k_{r1}$ ,  $k_{r2}$ ,  $n$ ,  $\tau$ , and  $\beta_f$  are shown in Table 4.

TABLE 4. Model Results of the Batch Reactor Experiments

expt no.	best-fit parameter values <sup>a</sup>					model efficiency		
	$k_{r1}$ (mM <sup>-1</sup> h <sup>-1</sup> )	$k_{r2}$ (mM <sup>1-n</sup> h <sup>-1</sup> )	$n$	$\tau$	$\beta_f$	$E_{Fe2}$	$E_{Fe3}$	$E_{Mn2}$
1	5.19 (0.17)	0.227 (0.046)	2.19 (0.16)	0.90 (0.14)	$0.95 \times 10^{-3}$ ( $0.31 \times 10^{-3}$ )	0.9990	0.9914	0.9987
2	2.35 (0.18)	0.554 (0.122)	1.84 (0.22)	2.94 (0.56)	$1.15 \times 10^{-3}$	0.9981	0.9913	0.9934
3	6.71 (0.38)	0.398 (0.175)	1.78 (0.37)	1.72 (0.47)	$1.15 \times 10^{-3}$	0.9984	0.9926	0.9973
4	8.58 (0.47)	0.120 (0.067)	2.46 (0.17)	0.20 (0.06)	$1.15 \times 10^{-3}$	0.9989	0.9956	0.9985
5	2.41 (0.14)	0.260 (0.073)	2.46 (0.17)	0.42 (0.05)	$1.15 \times 10^{-3}$	0.9972	0.9954	0.9941
6	3.21 (0.23)	0.461 (0.150)	1.83 (0.22)	0.55 (0.13)	$1.15 \times 10^{-3}$	0.9975	0.9839	0.9968
7	4.73 (0.25)	0.063 (0.040)	2.09 (0.57)	6.38 (1.37)	$1.15 \times 10^{-3}$	0.9995	0.9965	0.9892
8	2.10 (0.12)	0.150 (0.032)	2.48 (0.17)	3.90 (0.53)	$1.22 \times 10^{-3}$ ( $0.18 \times 10^{-3}$ )	0.9993	0.9917	0.9992
9	2.02 (0.01)	0.260 (0.028)	2.31 (0.03)	1.94 (0.20)	$1.30 \times 10^{-3}$ ( $0.56 \times 10^{-3}$ )	0.9995	0.9923	0.9963
10	2.03 (0.15)	0.879 (0.252)	1.48 (0.20)	1.97 (0.31)	$1.15 \times 10^{-3}$	0.9992	0.9923	0.9897

<sup>a</sup> Values in italics were not adjusted in the model inversion but determined from the average of experiments 1, 8, and 9. The standard errors of the parameter estimates are given in parentheses. The 95% confidence limits can be calculated from the standard error of the parameter estimate ( $\sigma$ ) as  $PE \pm 1.96\sigma$ , where PE is the best-fit parameter estimate.

of  $\tau$  exceed unity for six of the 10 experiments and average  $2.1 \pm 1.9$  across all experiments (Table 4), suggesting that a unit mass of Fe(III)(s) precipitate occluded a disproportionately large mass of MnO<sub>2</sub>. This is probably due to differences in the surface area-to-volume ratio of the two solid phases, with Fe(III)(s) present as thin coatings, and the  $\beta$ -MnO<sub>2</sub> present as hemispherical particles (14). Despite the ability of the blocking function to mimic the link between precipitate formation and reductive-dissolution inhibition, the inter-treatment variability in  $\tau$  is significant (Table 4). This variation is not accounted for at present, but it does suggest that the blocking mechanism is a more complex function of the Fe(III)(s) and  $\beta$ -MnO<sub>2</sub>(s) concentrations than currently represented by eq 4 and, in particular, that  $\beta$  depends nonlinearly on the [Fe(III)(s)]-to-[ $\beta$ -MnO<sub>2</sub>(s)] ratio.

The parameter  $\beta_f$  exhibits remarkably small between-treatment variation for the three long-term experiments (16% relative standard deviation for experiments 1, 8, and 9), and a single  $\beta_f$  value describes reductive-dissolution in the seven short-term experiments (Table 4).  $\beta_f$  constrains the minimum level of reductive dissolution and equals the ratio of  $k_{rf}$ , an effective rate coefficient for late-stage reductive dissolution, to  $k_{r1}$ , the rate coefficient for reductive dissolution on a clean, unreacted  $\beta$ -MnO<sub>2</sub> surface. The magnitude of  $\beta_f$  ( $\sim 10^{-3}$ ) suggests large differences in the oxidative potential between reacted, coated and unreacted, uncoated  $\beta$ -MnO<sub>2</sub> surfaces and illuminates the important role of Fe(III)(s) precipitate formation in reducing the rates of  $\beta$ -MnO<sub>2</sub> reductive dissolution.

The kinetics of ferric iron precipitation on the  $\beta$ -MnO<sub>2</sub> surface are approximately second-order with respect to Fe(III)(aq) concentration, with the average value of  $n$  equal to  $2.1 \pm 0.3$  (Table 4). These results imply that Fe(III) precipitation on  $\beta$ -MnO<sub>2</sub> is more complicated than the first-order dependence on Fe(OH)<sub>3</sub>(aq) concentration observed for the homogeneous precipitation of ferrihydrite at pH 3 in the presence of chloride (25). The optimal values of the rate coefficient for Fe(III)(aq) precipitation ( $k_{r2}$ ) average  $0.34 \text{ mM}^{1-n} \text{ h}^{-1}$  for the 10 experimental treatments (Table 4) and range from  $0.063 \text{ mM}^{1-n} \text{ h}^{-1}$  to  $0.879 \text{ mM}^{1-n} \text{ h}^{-1}$ . This between-treatment variation in  $k_{r2}$  indicates that eq 10 represents an apparent, rather than mechanistic, rate law.

Nevertheless, the optimal  $k_{r2}$  values are generally tightly clustered, as the 95% confidence intervals calculated from the standard errors of the  $k_{r2}$  estimates overlap for seven of the 10 experimental treatments (see Table 4 for parameter standard errors).

**Implications to Aquifer Fate and Transport.** What do these findings regarding the inhibitory effects of reaction-product formation on reductive dissolution imply for the transport of redox-sensitive metals in groundwater? We addressed this question in a preliminary way by constructing a simple transport model and by using this model to simulate the movement of iron and manganese through a 50-m long strip of aquifer.

The model solves eqs 6–10 for MnO<sub>2</sub> reductive dissolution and Fe(III)(aq) precipitation, together with coupled equations for the one-dimensional transport of Fe(II)(aq), Fe(III)(aq), and Mn(II)(aq). Two simulations were conducted, one without reaction-product inhibition ( $\tau = 0$ ) and one with reaction-product inhibition ( $\tau = 2.1$ ). For both simulations, the porewater velocity was assumed equal to 1 m/d, and the average values of  $k_{r1}$ ,  $k_{r2}$ ,  $n$ , and  $\beta_f$  from the 10 batch experiments (see Table 4) were used to calculate the temporal changes in metals concentrations (breakthrough curves) 50 m downgradient from a continuous source of Fe(II)-containing groundwater. The goal of this modeling exercise is to illustrate the spatial and temporal influence of ferric precipitates on the rate of reductive dissolution of MnO<sub>2</sub>. As our rate constants were determined at pH 3, this exercise cannot address how the reaction rates change with pH.

The breakthrough curves calculated in response to the Fe(II) injection differ markedly between the two scenarios considered (Figure 5), suggesting that the groundwater transport of Fe(II), Mn(II), and Fe(III) is very sensitive to the reaction-inhibition process measured in our batch experiments. Breakthrough of Fe(II) occurs earlier in the simulation with oxidation–reduction inhibition because Fe(III)(s) precipitate formation accelerates the decline in MnO<sub>2</sub> oxidative capacity, leading to incomplete conversion of Fe(II) to Fe(III) along the flow path. The reaction-inhibition process also lowers the concentrations of Mn(II) and Fe(III), the aqueous-phase products of reductive dissolution, and supports a prolonged period of slow oxidation–reduction kinetics, which

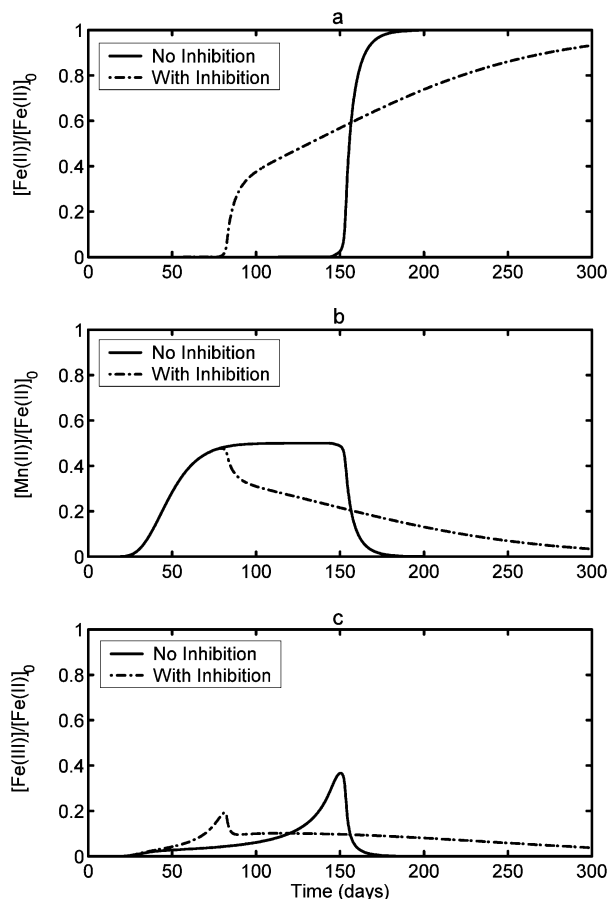


FIGURE 5. Simulated breakthrough curves for (a) Fe(II), (b) Mn(II), and (c) Fe(III) for scenarios with and without reaction-product inhibition. Concentrations of Mn(II) and Fe(III) were generated from the reductive-dissolution reaction (i.e., reaction 1), as only Fe(II) was present at the source location. The breakthrough concentrations are normalized to  $[\text{Fe(II)}]_0$ , the Fe(II)(aq) concentration at the seepage source. We assumed an average linear porewater velocity of 1 m/d, so the groundwater travel time through the 50-m strip of aquifer equaled 50 days.

is reflected by the comparatively gradual increase in Fe(II) concentrations (following initial breakthrough) and the long tails on the Mn(II) and Fe(III) breakthrough curves.

Comparison of these model results with those performed by Brown et al. (26) on the reductive-dissolution of pyrolusite by Fe(II) in the Pinal Creek Basin aquifer reveals a common feature of a peak in Mn(II) concentration. The release of Mn(II) continues at a much higher rate in our simulations than those done by Brown et al. (26), however. This was expected because our model does not account for the effects of pH changes on reactions rates. Results from Postma (11) show that the rate of reductive dissolution of birnessite decreases as the pH increases from 3 to 6. Other factors that may affect the shapes of the breakthrough curves include (1) Mn(II) adsorption to mineral surfaces due to the down-gradient pH increase, (2) the precipitation of rhodochrosite ( $\text{MnCO}_3$ ) as included in the model of Brown et al. (26), and (3) the formation of a mixed Mn-Fe constituent ( $\text{MnFe}_2\text{O}_4$ ) such as proposed by Villinski et al. (27).

Oxidation of other metals, in addition to Fe(II), is influenced by the formation of reaction-products that occlude the redox-reactive surface. Inhibition of Cr(III) and Co(II) oxidation, for example, has been widely cited and has been attributed to reaction-products that poison the  $\text{MnO}_2$  surface (23, 28, 29). These published studies, when taken in context to our transport simulations, suggest that accurate prediction

of the subsurface fate and distribution of a broad class of redox-sensitive contaminants will rely on modeling approaches that, like ours, explicitly link oxidation-reduction kinetics to the concentrations of products generated by these reactions.

## Acknowledgments

This research was made possible by Grant numbers P42 ESO4940 (National Institute of Environmental Health Sciences to M.H.C.) and CHE-9905654 (National Science Foundation to M.H.C.) and performed under appointment to the Environmental Restoration/Waste Management Graduate Fellowship Program administered by Oak Ridge Institute for Science and Education for the United States Department of Energy (J.E.V.). A grant from the NSF's Hydrological Sciences Program (EAR-990958) supported J.E.S. for his work on this manuscript.

## Supporting Information Available

Information regarding the identification of the manganese coating on the quartz substrate and SEM micrographs of the  $\beta\text{-MnO}_2$  coated quartz before and after reaction with Fe(II). This material is available free of charge via the Internet at <http://pubs.acs.org>.

## Literature Cited

- (1) Sass, B. M.; Rai, D. *Inorg. Chem.* **1987**, *26*, 2228–2232.
- (2) Eary, L. E.; Rai, D. *Environ. Sci. Technol.* **1987**, *21*, 1187–1193.
- (3) Rai, D.; Sass, B. M.; Moore, D. A. *Inorg. Chem.* **1987**, *26*, 345–349.
- (4) Oscarson, D. W.; Huang, P. M.; Defosse, C.; Herbillo, A. *Nature* **1981**, *291*, 50–51.
- (5) Moore, J. N.; Walker, J. R.; Hayes, T. H. *Clays Clay Miner.* **1990**, *38*, 549–555.
- (6) Tournassat, C.; Charlet, L.; Bosbach, D.; Manceau, A. *Environ. Sci. Technol.* **2002**, *36*, 493–500.
- (7) Stollenwerk, K. G. *Appl. Geochem.* **1994**, *9*, 353–369.
- (8) Stone, A. T.; Morgan, J. J. In *Aquatic Surface Chemistry: Chemical Processes at the Particle-Water Interface*; Stumm, W., Ed.; John Wiley & Sons: New York, 1987; pp 221–254.
- (9) Nesbitt, H. W.; Canning, G. W.; Bancroft, G. M. *Geochim. Cosmochim. Acta* **1998**, *62*, 2097–2110.
- (10) Banerjee, D.; Nesbitt, H. W. *Geochim. Cosmochim. Acta* **1999**, *63*, 1671–1687.
- (11) Postma, D. *Geochim. Cosmochim. Acta* **1985**, *49*, 1023–1033.
- (12) Fendorf, S.; Jardine, P. M.; Patterson, R. R.; Taylor, D. L.; Brooks, S. C. *Geochim. Cosmochim. Acta* **1999**, *63*, 3049–3057.
- (13) Stahl, R. S.; James, B. R. *Soil Sci. Soc. Am. J.* **1991**, *55*, 1291–1294.
- (14) Villinski, J. E. Thesis, The University of Arizona, 2001.
- (15) Hem, J. D. In *Particulates in Water*; Kavanaugh, M. C., Ed.; Advances in Chemistry Series 189; American Chemical Society: Washington, DC, 1980; pp 45–72.
- (16) Khang, S. J.; Levenspiel, O. *Chem. Eng. Sci.* **1976**, *31*, 569–577.
- (17) Tamura, H.; Goto, K.; Yotsuyanagi, T.; Nagayama, M. *Talanta* **1974**, *21*, 314–318.
- (18) Stumm, W.; Morgan, J. J. *Aquatic Chemistry: Chemistry Equilibria and Rates in Natural Waters*; Wiley: New York, 1996; p 780.
- (19) Crerar, D. A.; Barnes, H. L. *Geochim. Cosmochim. Acta* **1974**, *38*, 279–300.
- (20) Bigham, J. M.; Schwertmann, U.; Carlson, L.; Murad, E. *Geochim. Cosmochim. Acta* **1990**, *54*, 2743–2758.
- (21) Saiers, J. E.; Guha, H.; Jardine, P.; Brooks, S. *Water Resour. Res.* **2000**, *36*, 3151–3165.
- (22) Guha, H.; Saiers, J. E.; Brooks, S.; Jardine, P.; Jayachandran, K. *J. Contam. Hydrol.* **2001**, *49*, 311–334.
- (23) Allison, J. D.; Brown, D. S.; Novo-Gardac, K. J. MINTEQA2/PRODEFA2, A geochemical assessment model for environmental systems: Version 3.0 manual. U.S.EPA document EPA/600/3-91/021; 1991; p 106.
- (24) Press, W. H.; Flannery, B. P.; Teukolsky, S. A.; Vetterling, W. T. *Numerical Recipes: The Art of Scientific Computing*; Cambridge University Press: New York, 1986; p 818(22).

- (25) Grundl, T.; Delwiche, J. *J. Contam. Hydrol.* **1993**, *14*, 71–97.
- (26) Brown, J. G.; Bassett, R. L.; Glynn, P. D. *J. Hydrol.* **1998**, *209*, 225–250.
- (27) Villinski, J. E.; O'Day, P. A.; Corley, T. L.; Conklin, M. H. *Environ. Sci. Technol.* **2001**, *35*, 1157–1163.
- (28) Fendorf, S. E.; Zasoski, R. J.; Burau, R. G. *Soil. Sci. Soc. Am. J.* **1993**, *57*, 1508–1515.
- (29) Jardine, P. M.; Taylor, D. L. *Geochim. Cosmochim. Acta* **1995**, *59*, 4193–4203.

*Received for review January 22, 2003. Revised manuscript received September 11, 2003. Accepted September 23, 2003.*

ES034060R